
QT-Net: Rethinking Evaluation of AI Models in Atomic Chemical Space

Pablo Martínez Crespo

Department of Computer Science and Engineering
Chalmers University of Technology and University of Gothenburg
pabloma@chalmers.se

Stefano Ribes

Department of Computer Science and Engineering
Chalmers University of Technology and University of Gothenburg

Martin Rahm

Department of Chemistry and Chemical Engineering
Chalmers University of Technology

Richard Beckmann

Department of Computer Science and Engineering
Chalmers University of Technology and University of Gothenburg

Robert S. Jordan

Technology Research
Intel Corporation

Marisa Gliège

Chief Technology Office
EMD Electronics

Santiago Miret

Lila Sciences

Vijay Kris Narasimhan

Chief Technology Office
M Ventures

Rocío Mercado

Department of Computer Science and Engineering
Chalmers University of Technology and University of Gothenburg
rocio.mercado@chalmers.se

Abstract

Atomic properties such as partial charges or multipoles encode chemically meaningful information that can inform downstream molecular property prediction, but their evaluation as machine learning targets has been complicated by the absence of a principled out-of-distribution evaluation protocol at the atomic level. In this work, we propose a held-out evaluation protocol that clusters atomic environments by SOAP descriptors and computes metrics accounting only for cluster labels unseen during training. Following this procedure, we use 5×5 cross-validation and Tukey’s HSD to run a statistically rigorous comparison of E(3)-equivariant against non-equivariant, rotationally augmented models for predicting electron populations and multipoles of H, C, N, and O atoms. Building on our results, we introduce the Quantum Topological Neural Network (QT-Net), a rotationally augmented, non-equivariant graph neural network. We show that QT-Net can be used to infer properties of atoms in molecules from QM9 outside our training set, and that these inferred properties can yield improvement when used as input features for downstream molecular property prediction. To further validate the framework, molecular dipole moments computed from QT-Net’s per-atom outputs recover the ground-truth values reported in QM9. We release all code and data, including a JAX implementation of QT-Net, to support the broader use of learned QTA properties as inductive biases for atomic-scale molecular machine learning.

1 Introduction

Molecular property prediction[21, 31], accelerated simulations[20, 22], and *de novo* molecular design[40, 15] are among the main drivers of new artificial intelligence (AI) for science methods. However, out-of-distribution (OOD) generalization and broad sampling are among the most pressing challenges in the field. [11, 35, 2] Molecular representations built from first principles atomic properties are a promising avenue for tackling this research gap. [18, 36, 14, 23, 1]

Because atoms in molecules and materials interact as open quantum systems that exchange energy and charge with their neighbors, not all atoms of the same element can be treated as equal. Quantum chemists have developed several atomic descriptors that can also be effective for downstream property prediction, including conceptual density functional theory (DFT) reactivity indices such as Fukui functions [30], electrostatic surface potentials and local ionization energies [18], natural population analysis [36], interacting quantum atoms (IQA) energy decompositions [25, 7, 16], and the various definitions of atomic partial charge [27, 39, 5, 9]. Works by Vargas et al. [37] and Gee et al. [13] showed that descriptors derived from the quantum theory of atoms in molecules (QTAIM) can enhance regression tasks such as predicting activation energies in reactions, or formation and orbital energies of transition metal complexes with less than 1 000 training points. Recently, the AIMEL dataset [28], a subset of QM9 [33] with quantum topological atomic (QTA) properties for H, C, N and O such as electron populations, multipole moments, and localization indices, was released. Some open questions from these works are whether QTA properties inferred by a model would preserve their predictive power, and which properties are the most informative outside the region of chemical space that a model was trained on.

Several studies have focused on learning atomic partial charges and multipoles derived from first-principles. [27, 19, 39, 38, 5] Nevertheless, truly OOD evaluation is precluded by the usage of random splits, which cannot prevent atomic environments from leaking into test sets. Atoms, as the building blocks of chemistry and molecules, are open quantum systems with complex interactions of their own dictated by their electronic structure. In this work, we show that metrics that account for all atoms in a test set of molecules, rather than only atoms in environments unseen during training, lead to overconfident results that don't reflect true OOD performance.

In view of this, we introduce the Quantum Topological Neural Network (QT-Net) for learning QTA properties, a densely connected, non-equivariant graph neural network (GNN). To address the aforementioned limitations, our key contributions are:

- **Statistically significant benchmarking.** We apply repeated means-ANOVA (RM-ANOVA) and Tukey's honestly significant difference (HSD) frameworks for comparing E(3)-equivariant against non-equivariant multitask models to predict scalar and tensor properties for topological atoms.
- **Faithful OOD evaluation.** Our evaluation set, built upon per-element clustering of smooth overlap of atomic positions (SOAP), contains atomic environments unseen during training, and our metrics only account for atoms in said unseen environments.
- **Inferential quality assessment.** We infer QTA properties for all the QM9 atoms outside of AIMEL, and show that the molecular dipole moment is recovered from its atomic contributions.

2 Related work

A productive line of work has applied machine learning (ML) to QTA properties drawn from QTAIM, the IQA formalism, and related branches of quantum chemical topology (QCT), establishing that these chemical descriptors are within reach of modern regressors. Early contributions used Gaussian process regression to predict the full set of IQA energy components for small biomolecular fragments [25], and were subsequently extended to clusters with the formamide-dimer transfer-learning study of Brown et al. [7], which expanded the property catalog to atomic multipole moments. The works by Gallegos et al. [9, 10] introduced neural networks for predicting QTAIM atomic charges of H, C, N, and O atoms, and one-body and two-body QTAIM and IQA descriptors. Most recently, Hoffmann et al. [16] have shown that equivariant graph networks can learn IQA-decomposed atomic and pairwise energies across diverse benchmark sets. Together, these works establish QTA properties as a realistic ML target and have steadily expanded the space of accessible descriptors.

A methodological pitfall nevertheless recurs across this literature, bearing directly on the OOD-evaluation contribution we make in this work. Mainly, these works rely on splits that do not isolate unseen atomic environments. Maxwell et al. [25] and Gallegos et al. [9] draw their splits at random from a common pool of geometries, which is bound to leak atomic environments seen during training into the test set. Their follow-up [10] probes extrapolation along reaction coordinates and through a supramolecular trajectory — useful as configurational-space stress tests, but uninformative about generalization across chemical space. Brown et al. [7] sample training and evaluation from a single molecular-dynamics trajectory of the same monomer. They show that their monomer-trained multipoles fail to transfer to the dimer regime, providing perhaps the most clear signal that environment-level OOD is a standing challenge.

3 Methods

Figure 1 summarizes the methodology followed to train and evaluate the proposed QT-Net models.

3.1 Target properties of topological atoms

QTAIM defines an atom as a region in real space $\Omega \subset \mathbb{R}^3$ such that $\nabla\rho(\mathbf{r}) \cdot \hat{\mathbf{n}}(\mathbf{r}) = 0 \forall \mathbf{r} \in \partial\Omega$, where ρ is the electron density and $\hat{\mathbf{n}}(\mathbf{r})$ is the normal vector to the surface defined by $\partial\Omega$, meaning there is no flux of electrons through the boundary of the basin. Atomic properties depend on the shape of this basin, as they are quantities integrated over it. In this work, we focus on electron population (N), atomic contribution to molecular dipole moment ($\boldsymbol{\mu}$), traceless quadrupole moment (\mathbf{Q}), and localization index (λ),

$$N = \int_{\Omega} \rho(\mathbf{r}) d\mathbf{r}, \quad \boldsymbol{\mu} = - \int_{\Omega} e \mathbf{r}^{(\Omega)} \rho(\mathbf{r}) d\mathbf{r} + \sum_{\Lambda}^{N_b(\Omega)} [\mathbf{R}_{\Omega} - \mathbf{R}_b(\Omega|\Lambda)] q(\Omega|\Lambda),$$

$$\text{and } Q_{\alpha\beta} = - \int_{\Omega} e \rho(\mathbf{r}) \left(3r_{\alpha}^{(\Omega)} r_{\beta}^{(\Omega)} - \delta_{\alpha\beta} \|\mathbf{r}^{(\Omega)}\|^2 \right) d\mathbf{r}.$$

In the expressions above, $\rho(\mathbf{r})$ is the electron density, e is the charge of the electron, indices $\alpha, \beta \in \{x, y, z\}$ denote Cartesian components s.t. $r_{\alpha}^{(\Omega)}$ is the α component of the displacement from the nuclear position \mathbf{R}_{Ω} , $N_b(\Omega)$ is the number of bond critical points (BCPs) connected to atom Ω , $\mathbf{R}_b(\Omega|\Lambda)$ is the position of the BCP between atoms Ω and Λ and $q(\Omega|\Lambda)$ is the charge transfer between these atoms. The localization index λ is defined from the variance of the electron population within a basin as $\lambda = N - \sigma^2(N)$, and quantifies the extent to which electrons are localized within the basin Ω vs shared with neighboring basins. We refer the interested readers to the book by Matta and Boyd [24]. Here N is a scalar, $\boldsymbol{\mu}$ is a 3-vector, \mathbf{Q} is a rank-2 traceless symmetric tensor with 5 independent components, and λ is a scalar.

3.2 Dataset construction and atomic environments

We used the QTAIM atomic multipoles (N , $\boldsymbol{\mu}$, \mathbf{Q}) and localization indexes (λ) reported in AIMEL [28]. The AIMEL Zenodo repository [29] releases data in two formats: a summary .csv file covering approximately 40 000 molecules but containing only scalar properties, and per-molecule .sumviz files (raw AIMAll output) that include the full tensor components of $\boldsymbol{\mu}$ and \mathbf{Q} . To enable the comparison of equivariant and non-equivariant models on tensorial targets, we parsed the .sumviz files directly. These were available for 31 223 of the molecules, defining our working dataset.

To enable evaluation on atomic environments not seen during training, we group atoms into element-specific clusters of similar local environment, which are later used to construct held-out test sets of atoms whose cluster labels never appear in the training data. For each atom we computed the SOAP descriptors [3] (cutoff 8 Bohr, 8 radial basis functions, spherical harmonics up to $L = 6$, Gaussian smearing $\sigma = 0.7$ Bohr; 3696 features per atom). These were reduced using principal component analysis (PCA) to element-specific numbers of features preserving at least 99% of the variance, and clustered separately by atomic species using HDBSCAN [26]. Each atom in the dataset was then annotated with its element-centered environment label. Cluster statistics are reported in Table 4 and Figures 6 and 7 in the Appendix.

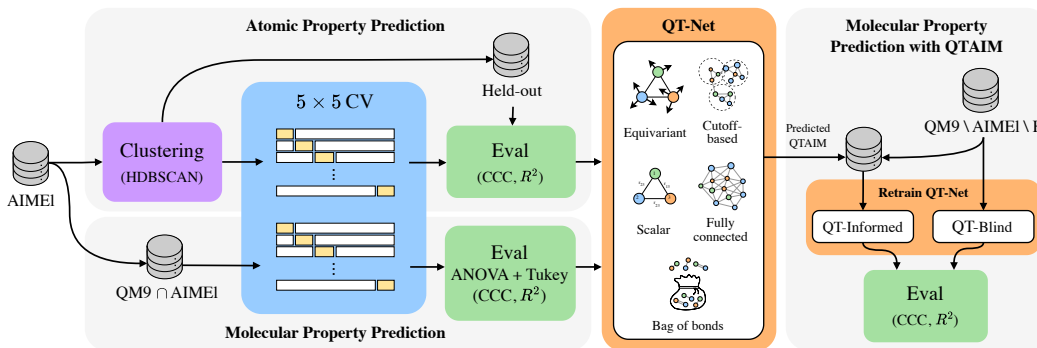


Figure 1: QT-Net training and evaluation pipeline on AIMEI for atomic (QTAIM) and molecular property prediction, together with QTAIM-informed and QTAIM-blind experiments on remaining QM9 molecules.

Because the AIMEI dataset is a subset of QM9 [33], we paired each molecule with its QM9-reported molecular properties, enabling later evaluation of how QTA-property information affects downstream molecular property prediction. We retained four target properties: isotropic polarizability (α), HOMO–LUMO energy gap (Δ), internal energy at 0 K (U_0), and heat capacity at 298.15 K (C_v). Together, these span both electrostatic-response and energetic properties, for which the estimation of atomic multipoles is plausibly informative. Following [33], we excluded from QM9 the 3 054 molecules reported to fail the geometry-consistency check (molecules whose DFT-optimized geometry does not match their input SMILES — flagged by the QM9 authors as a known issue). From AIMEI, we removed 411 entries with missing molecular property values. The resulting AIMEI-derived dataset contains 30 812 molecules.

We now describe the construction of the held-out set for the evaluation of QTA models. For reproducibility purposes, we use A_i in the following to refer to the label of an atomic environment centered around element A , as these are the labels reported with our dataset. We selected N_{13} first, as nitrogen was the limiting factor for holdout size; over 90% of molecules containing N_{13} also contained C_{11} and H_{10} , so both were added to prevent co-occurrence leakage. Including these three labels automatically absorbed all O_{10} -containing molecules, which we therefore retained as a fourth evaluation label at no additional cost in training-set size. The final test set contains 5 840 molecules, with at least one unseen cluster label per atom type (see Fig. 2), forming a coherent OOD region of chemical space at both the molecular and atomic levels.

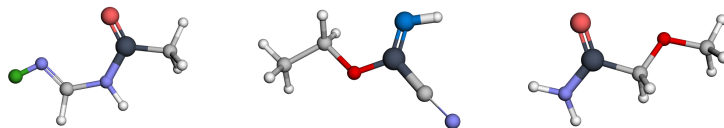


Figure 2: Sample molecules with held out atomic environments. From left to right: CC(=O)NC=N, CCOC(=N)C#N, and COCC(N)=O. Color for atoms in held out environments: H_{10} , C_{11} , N_{13} , O_{10} . Color for the other atoms: H, C, N, O.

For the molecular property prediction experiments, we included the QM9 molecules outside AIMEI, excluding those containing fluorine (as there was no data for it in AIMEI), yielding 98 096 molecules whose QTAIM properties were inferred using the trained models.

3.3 Cross-validation at the atomic level

All models are evaluated using a 5-repeat, 5-fold cross-validation (5×5 CV) protocol, yielding 25 fold-level scores per model. A standard 5×5 CV protocol computes performance metrics on a fold-specific holdout drawn at random from the data. Here, working for atomic properties in the data regime of the AIMEI dataset forces the usage of a common held-out set for all 25 folds. We justify this design in the Limitations (Sec. 6) and provide metrics of the statistical validity of the comparison in the Appendix A.4.

The molecules outside the test set are partitioned into fold-specific training and validation sets. Within each repeat, molecules are split into five folds using GroupKFold with the Bemis–Murcko scaffold as the grouping variable, so all molecules sharing a scaffold are assigned to the same fold; each fold’s validation set therefore contains only scaffolds entirely absent from the training set. Scaffold-to-fold assignments are re-shuffled with an independent seed at each repeat, making the five repeats statistically distinct.

3.4 Statistical framework of the model comparison

We compare model performance using a repeated-measures ANOVA (RM-ANOVA) with Tukey’s honestly significant difference (HSD) as the post-hoc pairwise test. Data limitations force a common hold-out set across all folds (Sec. 6), on which we compute per-fold concordance correlation coefficients (CCC) for each (holdout label, property). Because the five folds within a repeat share this hold-out and overlap in training data, their scores are correlated. We therefore average them into a single repeat-level score, yielding five approximately independent observations per model in a balanced design with repeat as subject and model as treatment. Means and 95% confidence intervals are reported as $\bar{x} \pm t_{0.975,4} \cdot \text{SEM}$, where SEM is the standard error of the five repeat-level means. Tukey HSD then defines a minimum significant difference (MSD) such that two models differ significantly iff the gap between their repeat-averaged means exceeds it.

Because the metric is averaged at the fold level before the repeat-level mean is taken, this average can be computed over any subset of (atom \times property) cells — e.g. hydrogen-only, dipole-norm pooled across atoms, or a single (atom, property) stratum — without altering the inferential structure. The MSD automatically tightens as more cells are pooled (smaller within-model variance). We verify normality (Shapiro–Wilk on the five repeat-level means per model) and across-model homoscedasticity (Levene’s test). See Section A.4. The intraclass correlation is near zero for all models, with effective sample sizes between 20 and 25 out of 25 raw folds — confirming that within-repeat fold scores are nearly independent and that the repeat-averaging step is conservative rather than load-bearing. Sphericity corrections (Mauchly / Greenhouse–Geisser) are therefore not needed.

3.5 The QT-Net architecture

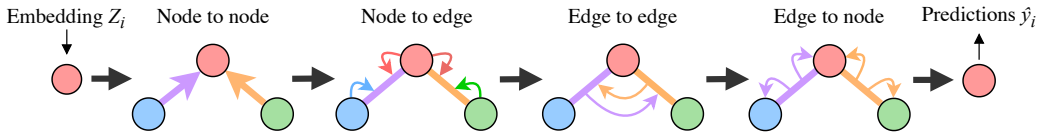


Figure 3: Schematic figure of a layer of message passing of QT-Net.

The set of transformations that compose a layer of QT-Net is represented in Figure 3. We focus on the transformations for the scalar versions of QT-Net, as that was the best-performing design. See Section A.8 for details on E(3)-equivariant models. Our architecture is inspired by the attention and gating mechanisms of the work by Irwin et al. [17], the separation of feature and geometric channels by Schütt et al. [34], and the chemical reminders, raw-component input, and per-layer readout by Pozdnyakov and Ceriotti [32].

We represent each atom by a node with scalar features h_i . For edge features, we follow the same convention, but with double subindexes (e.g., h_{ij}). We denote the element-wise (Hadamard) product with \odot . In the equations below that can apply to either type of cell, we absorb the subindexes of nodes and edges into the subscripts r , s , t to refer to receivers, senders and intermediaries (respectively). In messages between nodes, the intermediary would be the edge connecting them (and the common node between two edges for messages between edges). The usage of Hadamard product implies that the output dimension of MLPs and geometric filters match the number of features of the receiver. We use SiLU as activation function between hidden layers.

In all models, node features are initialized with a message passing layer as follows:

$$h_i^{(0)} = \text{LayerNorm} \left(\sum_j \text{MLP}(\text{EMBED}(Z_i), \text{EMBED}(Z_j)) \odot \Gamma(\hat{\mathbf{r}}_{ij}, \text{RBF}(r_{ij})) \right), \quad (1)$$

where Z_i, Z_j , are the atomic species. Γ is a geometric gate with tanh activation output that takes as input the components of the inter-atom displacement vector, concatenated to a projection onto radial basis functions (RBFs) as implemented in DimeNet [12]:

$$\text{RBF}_n(r) = \sqrt{\frac{2}{c}} \frac{\sin(n\pi r/c)}{r} \frac{1 + \cos(\pi r/c)}{2}.$$

Edge features are initialized from these node features as follows

$$h_{ij}^{(0)} = \text{LayerNorm} \left(\text{MLP} \left(\text{LayerNorm} \left(\sum_{k \in \{i,j\}} \text{MLP} \left(h_k^{(0)} \right) \right) \right) \odot \Gamma \left(\hat{\mathbf{G}}_{ij}, \text{RBF}(r_{ij}) \right) \right), \quad (2)$$

where $\hat{\mathbf{G}}_{ij} \propto \hat{\mathbf{r}}_{ij} \otimes \hat{\mathbf{r}}_{ij}^T$ is the edge’s normalized gyration tensor expressed in the traceless symmetric representation. See Section A.2.

After these, all layers follow a residual update structure, $h'_r = h_r + g(h_r) \odot M_r(\tilde{h}_r, \tilde{h}_s, \tilde{h}_t)$, where g is a gating MLP with a sigmoid output that depends on the unnormalized features, and $M_r(\tilde{h}_r, \tilde{h}_s, \tilde{h}_t)$ is a message aggregation with $\tilde{h}_r, \tilde{h}_s, \tilde{h}_t$ being LayerNormed receiver, sender, and intermediary features, respectively. In general,

$$M_r(\tilde{h}_r, \tilde{h}_s, \tilde{h}_t) = \sum_{s,t \in \mathcal{N}_t(r)} \text{MLP}(\tilde{h}_r, \tilde{h}_s, \tilde{h}_t) \odot \Gamma(\mathbf{R}_r, \mathbf{R}_s),$$

where $(\mathbf{R}_r, \mathbf{R}_s)$ is some real-space geometric relation between receiver and sender. In node-to-node and node-to-edge messages, we use the same convention as in Eqs. 1 and 2, respectively. In edge-to-edge messages, $(\mathbf{R}_r, \mathbf{R}_s) \equiv (\hat{\mathbf{G}}_{rs}, P(\cos[\mathbf{G}_r, \mathbf{G}_s]))$, where $\hat{\mathbf{G}}_{rs} = (\mathbf{G}_r - \mathbf{G}_s) / \|\mathbf{G}_r - \mathbf{G}_s\|$ is the unit-norm relative gyration tensor and we project $\cos(\mathbf{G}_r, \mathbf{G}_s) = \text{Tr}(\hat{\mathbf{G}}_r^T \hat{\mathbf{G}}_s)$ onto a basis of Legendre polynomials, $\{P_n(x)\}$, since the gyration tensors contain angular information.

At the end of a messaging cycle, we apply a feed-forward (FF) residual update following the expression

$$h'_r = h_r + g(h_r) \odot \text{MLP}(\tilde{h}_r, W \cdot \text{EMBED}(Z_r)),$$

where we include a linear transformation of the initial embedding of the atomic species to serve as a chemical reminder (but that term is omitted for edges’ FF).

Finally, the prediction of the model for the properties of a given atom, $\hat{y}_i = (\hat{N}_i, \hat{\lambda}_i, \hat{\boldsymbol{\mu}}_i, \hat{\mathbf{Q}}_i)$ is a readout that depends on an atomic head at the end of each layer:

$$\hat{y}_i^{(l)} = W \cdot \text{MLP} \left(\text{LayerNorm} \left(h_i^{(l)} \right) \right), \quad \text{and} \quad \hat{y}_i = \sum_l \alpha^{(l)} \hat{y}_i^{(l)},$$

where the layer weights α come from a softmax, $\alpha^{(l)} = \exp(\omega^{(l)}) / \sum_{l'} \exp(\omega^{(l')})$.

4 Experiments

4.1 Atomic property prediction

Our objective was to find out which architectural features offered the best tradeoff between computational cost and quality of inferred QTA properties with respect to the ground truth distribution. In order to find the best candidate for this inference task, we trained a series of E(3)-equivariant and non-equivariant models for QTA prediction, both with fully connected and cutoff based models, ensuring all atoms had at least 2 neighbors within cutoff (see Fig. 10). Hyperparameter optimization was run for a first batch of experiments, after which we further tuned width and depth of the models to keep sensible, matched compute cost across models (see Sec. A.1). We trained for a number of epochs between 1500 and 3000, keeping training wall-time below 2 days per fold. Nevertheless, all models plateaued after epoch 1000. The parameters with the lowest validation loss were used for each fold’s predictions.

Table 1: Architectural details of the main models in the discussion. E-models are equivariant. Data augmented models saw randomly rotated molecules every epoch.

Models	Architectural details			
	Cutoff (Bohr)	Max. n.n.	Depth (layers)	Data augmented
EGFC	-	-	4	-
SFC2	-	-	7	Yes
SGFC	-	-	7	No
SG-8-12	8	12	7	Yes
SG-8-5	8	5	7	Yes
EGNN	5.25	5	4	-
SGNN	5.25	5	7	No

4.2 Molecular properties from inferred QTA properties

We ran experiments on molecular property prediction on the AIMEL subset with a molecular version of QT-Net that omitted explicit geometric information, replaced the atomic heads for a molecular head, and used a 3.5 Bohr cutoff with 4 n.n. Each model was trained both with (‘informed’) and without (‘blind’) ground truth QTA properties as input. Again, the 5×5 CV protocol was followed, this time with a different holdout per fold based on the Bemis–Murcko scaffolds. We compared several metrics with and without QTA input at different training fractions. Each fold was split into 70% training, 10% validation and 20% test, keeping validation and test fixed across training fractions. The training fraction was extracted from the 70% pool.

An ensemble of 5 models with the selected QT-Net architecture was re-trained on the whole ground truth in AIMEL, having different validation sets for each member of the ensemble for early stopping. We use this ensemble to infer QTA properties for each of the atoms in the remainder of QM9. The quality of the multipoles and localization indexes inferred by this ensemble was tested by two different experiments. In the first, the performance of both molecular models previously trained on the AIMEL subset was compared on the remainder of the QM9 dataset, with the inferred properties by QT-Net as input for the informed variant. We make ensemble molecular predictions of 5 informed vs 5 blind models, selecting the best performing model of each repeat. In the second experiment, we directly sum the inferred atomic contributions to the molecular dipole moments, and compared the resulting molecular dipole moments against the ground truth in QM9.

5 Discussion

5.1 Model comparison on OOD atomic environments

For each model, element, and QTA property, we report Lin’s concordance correlation coefficient (CCC), defined as $\rho_c = 2 \text{Cov}(y, \hat{y}) / (\sigma_y^2 + \sigma_{\hat{y}}^2 + (\mu_y - \mu_{\hat{y}})^2)$. This metric jointly penalizes deviations from the identity line and mean bias, making it more sensitive to always-positive quantities such as $|\mu|$ and $|\mathbf{Q}|$. Our discussion revolves around the interplay among cutoff, number of nearest neighbors (n.n.) and architectural constraints. The statistical validity of the comparison gets slightly compromised when digging into the peculiarities of each species, and therefore we defer this part of the discussion to Section A.6. More architectures were tested (including topological message passing [6, 8] and tensor product layers), which offered no advantage at increased computational cost. Interested readers are referred to the repository for more information.

The results in Table 2 show that non-equivariant, rotationally augmented models outperform the equivariant counterparts significantly. Looking at Table 1, one would be tempted to attribute this advantage to the greater depth of the scalar models. We argue that this depth is not being invested in passing chemical information, but rather in polishing the purely geometrical information that equivariant models understand by design. Interested readers are referred to Appendix Section A.6, where we discuss this possibility based on results from non-augmented models.

With the effect of the layer depth aside, the results suggest that the connectivity beyond 5 neighbors is mostly providing the non-equivariant models with geometric information, rather than chemical. On

Table 2: Tukey p-value matrix for CCC values averaged over atom types and properties, comparing data augmented, non-equivariant models with equivariant models. Values above 0.05 (marked in **bold**) indicate a statistically insignificant difference in performance. The best performing models are determined based on CCC mean value and statistical significance of the difference: 1st 2nd 3rd .

Models	Tukey p-values					CCC \pm 95% CI
	EGFC	SFC2	SG-8-12	SG-8-5	EGNN	
EGFC	1.0000	0.0010	0.0010	0.5729	0.0010	0.798 \pm 0.006
SFC2	0.0010	1.0000	0.8968	0.0010	0.0010	0.895 \pm 0.006
SG-8-12	0.0010	0.8968	1.0000	0.0010	0.0010	0.888 \pm 0.006
SG-8-5	0.5729	0.0010	0.0010	1.0000	0.0010	0.809 \pm 0.013
EGNN	0.0010	0.0010	0.0010	0.0010	1.0000	0.754 \pm 0.028

the one hand, notice that SG-8-5 performs on-par with EGFC. On the other, SG-8-12 outperforms EGFC and matches SFC2. Therefore, the increased amount of neighbors of SG-8-12 against SG-8-5 is helping the model achieve better geometric awareness, which doesn’t improve beyond 12 neighbors. Given this results, we chose the SG-8-12 architecture for QT-Net.

5.2 Quality of the inferred QTA properties

Our results for molecular property prediction on the AIMEL dataset are found in Section A.7. Therein, we show that the performance gain from ground truth QTA properties-informed models is statistically significant based on Table 10, and show the R^2 learning curves in Figure 11. The discussion below hence focuses on tasks that take as input inferred QTA properties. We use the averaged ensemble prediction to compute R^2 , then quantify its uncertainty with a non-parametric bootstrap over molecules (1000 resamples with replacement), reporting the 2.5–97.5% quantiles of the resampled R^2 distribution as the 95% confidence interval.

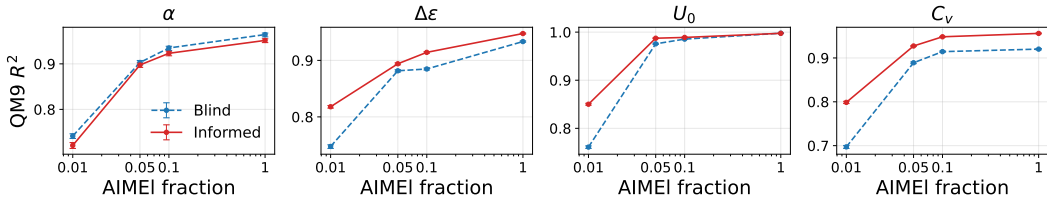


Figure 4: R^2 scores of ensembles of informed and blind models trained on different fractions of the data in AIMEL, when deployed on the remainder of QM9. Notice that these are not learning curves.

The plots in Figures 4 and 12 show that, even when trained on fewer than 300 molecules, both informed and uninformed ensembles achieve $R^2 > 0.7$ when deployed on the remainder of QM9. We notice that both ensembles perform on par for α , whereas there’s a systematic gain for $\Delta\epsilon$ and C_v . For U_0 , the performance gain from QTA properties is most noticeable at 1% training fraction.

Finally, we show a physics-based test where we directly computed the molecular dipole moments from the atomic contributions to the molecular dipole moment inferred by QT-Net. Following Matta and Boyd [24], the molecular dipole moment can be directly computed from the output of QT-Net for each atom Ω as

$$\boldsymbol{\mu} = \sum_{\Omega} \boldsymbol{\mu}(\Omega).$$

The result in Fig. 5 shows that QT-Net can predict properties of topological atoms outside of AIMEL. As a matter of fact, the observed outliers suggest that QM9 contains atoms in regions of atomic chemical space far from those in AIMEL. This recovery is a strong physical consistency check: because molecular dipole moments arise from the vector sum of per-atom contributions, accurate reconstruction requires that QT-Net has correctly learned not only the magnitudes but also the

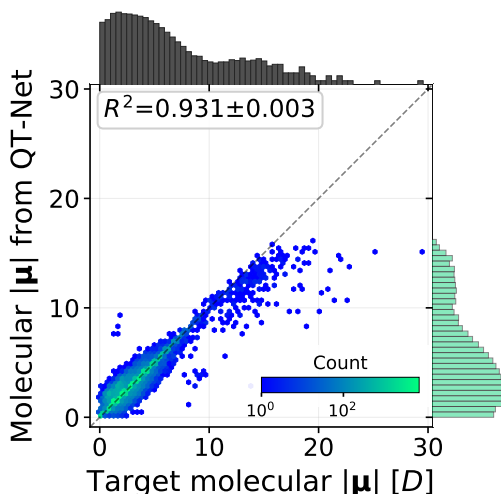


Figure 5: Parity plot for the molecular dipole moments on the remainder of QM9, computed from the atomic contributions inferred by QT-Net.

orientations of the inferred atomic dipoles relative to one another. That this physical relationship is preserved across $\sim 98\,000$ unseen QM9 molecules *without QT-Net ever having been trained to predict molecular dipoles directly* indicates that the model has captured the underlying QTAIM partitioning of the electron density rather than memorizing statistical regularities of the AIMEL distribution. This supports the broader use of QT-Net’s inferred QTA properties as physically meaningful inputs for downstream tasks.

6 Limitations

Here, we justify the usage of a common held-out set for evaluating the 25 folds of the models in Section 5.1. In standard molecular benchmarks, scaffolds are randomly assigned to folds, so the expected test-set difficulty is approximately equal across folds. Between-fold variance therefore reflects sampling noise, and the ANOVA exchangeability assumption holds approximately. At the atomic level, atomic environments play the role of “scaffolds”, but they co-occur within molecules: specific cluster labels are mutually enriched, so the presence of one label in a molecule raises the probability of finding another.

During training, showing the model an atomic label that is highly enriched with a held-out label would expose the model to atomic environments that co-reside in the same molecules as the held-out environments, allowing it to learn their structural context indirectly. Mutually enriched label sets must therefore be withheld together as a unit. In the AIMEL data regime, this constraint severely limits the number of admissible holdout combinations and precludes randomizing label assignments across repeats.

As a result, the Tukey HSD comparisons presented in this work are conditional on the chosen holdout and cannot be interpreted as claims of general OOD superiority of either design, neither of general superiority of non-equivariant over E(3)-equivariant models. We use them as guidance for deciding on the final QT-Net design for the inference and downstream tasks.

7 Conclusion

Our work shows a statistically thorough analysis of the performance difference between E(3)-equivariant and purely scalar, rotationally augmented models for the task of learning scalar and tensorial QTA properties. Our results suggest that scalar models benefit from densely connected graphs for capturing geometrical information, especially when data augmentation is used. We therefore justify a non-equivariant design for the introduced architecture, QT-Net, which we demonstrate

can reconstruct molecular dipole moments outside the set of training molecules from inferred atomic contributions.

We want to emphasize that OOD evaluation of AI models for QTA properties requires careful labeling and tracking of the atomic environments. The properties of an atom depend on its environment, and the same element can appear in chemically distinct environments within a molecule. Our approach shows that SOAP-based clustering can separate these chemically different environments, and enables us to construct OOD splits by withholding molecules that contain environments absent from the training set. Furthermore, using metrics that specifically measure model performance on these unseen environments enables us to design an architecture based on faithful metrics of OOD performance. Additional results in Section A.6 (specifically in Fig. 9) show that metrics that account for all atoms in a set of test molecules lead to overconfident results that do not evaluate the true OOD performance. This is a pitfall that has been repeatedly observed in the AI-for-QCT literature (see Section 2).

Our results suggest that further progress on QTA property prediction is now primarily a data problem rather than a representation or architectural challenge: across the four properties studied here, the same architecture achieves CCC values ranging from ~ 0.4 to ~ 0.99 depending on element and property, indicating that the bottleneck has shifted from how to model these targets to which targets to model and on what chemistry. Extending the framework introduced here to other quantum-mechanically derived atomic descriptors — such as conceptual DFT reactivity indices, natural bond orbital populations, IQA decompositions — and to broader regions of chemical space is, in our view, the natural next step.

8 Code and data availability

Code and data for this project are available at <https://github.com/pablomcrespo/QT-Net>. It includes all seeds and information to reproduce the experiments of this work, besides relevant code to reproduce the statistical analysis. The source data is referenced in the text, but we include compressed versions of our curated files (mainly for reproducibility with the same cluster labels). The QTAIM properties inferred by QT-Net are released in the repository, too.

Acknowledgments and Disclosure of Funding

PMC and RB acknowledge funding from the Intel-Merck joint university research center for AI-Aware Pathways to Sustainable Semiconductor Process and Manufacturing Technologies (AWASES). RM acknowledges funding provided by the Wallenberg AI, Autonomous Systems, and Software Program (WASP), supported by the Knut and Alice Wallenberg Foundation. PMC acknowledges Lynne Ressel for the inspiration in naming QT-Net. The computations and data storage were enabled by resources provided by Chalmers e-Commons and by the National Academic Infrastructure for Supercomputing in Sweden (NAISS), partially funded by the Swedish Research Council through grant agreement no. 2022-06725. The authors declare no competing interests.

References

- [1] Javier E Alfonso-Ramos, Rebecca M Neeser, and Thijs Stuyver. Repurposing quantum chemical descriptor datasets for on-the-fly generation of informative reaction representations: Application to hydrogen atom transfer reactions. *Digital Discovery*, 3(5):919–931, 2024.
- [2] Evan R Antoniuk, Shehtab Zaman, Tal Ben-Nun, Peggy Li, James Diffenderfer, Busra Sahin, Obadiah Smolenski, Tim Hsu, Anna M Hiszpanski, Kenneth Chiu, et al. BOOM: Benchmarking out-of-distribution molecular property predictions of machine learning models. *arXiv preprint arXiv:2505.01912*, 2025.
- [3] Albert P Bartók, Risi Kondor, and Gábor Csányi. On representing chemical environments. *Physical Review B—Condensed Matter and Materials Physics*, 87(18):184115, 2013.
- [4] Ilyes Batatia, Dávid Péter Kovács, Gregor N. C. Simm, Christoph Ortner, and Gábor Csányi. MACE: Higher order equivariant message passing neural networks for fast and accurate force fields, 2023. URL <https://arxiv.org/abs/2206.07697>.
- [5] Tristan Bereau, Denis Andrienko, and O Anatole Von Lilienfeld. Transferable atomic multipole machine learning models for small organic molecules. *Journal of Chemical Theory and Computation*, 11(7): 3225–3233, 2015.
- [6] Cristian Bodnar, Fabrizio Frasca, Nina Otter, Yuguang Wang, Pietro Lio, Guido F Montufar, and Michael Bronstein. Weisfeiler and Lehman go cellular: CW networks. *Advances in Neural Information Processing Systems*, 34:2625–2640, 2021.
- [7] Matthew L Brown, Bienfait K Isamura, Jonathan M Skelton, and Paul LA Popelier. Incorporating noncovalent interactions in transfer learning gaussian process regression models for molecular simulations. *Journal of Chemical Theory and Computation*, 20(14):5994–6008, 2024.
- [8] Pablo Martínez Crespo, Robert S. Jordan, Marisa Gliege, Santiago Miret, Vijay Kris Narasimhan, and Rocío Mercado. Topomole: Topological message passing meets hyperedge messages. In *AI for Accelerated Materials Design - NeurIPS 2025*, 2025. URL <https://openreview.net/forum?id=k39fE6SD4u>.
- [9] Miguel Gallegos, Jose Manuel Guevara-Vela, and Ángel Martín Pendás. NNAIMQ: A neural network model for predicting QTAIM charges. *The Journal of Chemical Physics*, 156(1), 2022.
- [10] Miguel Gallegos, Valentin Vassilev-Galindo, Igor Poltavsky, Ángel Martín Pendás, and Alexandre Tkatchenko. Explainable chemical artificial intelligence from accurate machine learning of real-space chemical descriptors. *Nature Communications*, 15(1):4345, 2024.
- [11] Wenhao Gao, Tianfan Fu, Jimeng Sun, and Connor Coley. Sample efficiency matters: A benchmark for practical molecular optimization. *Advances in Neural Information Processing Systems*, 35:21342–21357, 2022.
- [12] Johannes Gasteiger, Janek Groß, and Stephan Günnemann. Directional message passing for molecular graphs. *arXiv preprint arXiv:2003.03123*, 2020.
- [13] Winston Gee, Abigail Doyle, Santiago Vargas, and Anastassia N Alexandrova. Multi-level qtaim-enriched graph neural networks for resolving properties of transition metal complexes. *Digital Discovery*, 4(11): 3378–3388, 2025.
- [14] Yanfei Guan, Connor W Coley, Haoyang Wu, Duminda Ranasinghe, Esther Heid, Thomas J Struble, Lagnajit Pattanaik, William H Green, and Klavs F Jensen. Regio-selectivity prediction with a machine-learned reaction representation and on-the-fly quantum mechanical descriptors. *Chemical Science*, 12(6): 2198–2208, 2021.
- [15] Jiazhen He, Helen Lai, Lakshidaa Saigiridharan, Gian Marco Ghiandoni, Kinga Jenei, Umur Gokalp, Ajsa Nukovic, Ola Engkvist, Jon Paul Janet, and Samuel Genheden. Democratising real-world drug discovery through agentic ai. *Drug Discovery Today*, page 104605, 2026.
- [16] M Hoffmann, A Kazimir, T Oestereich, L Kaermer, F Engelberger, J Meiler, and C Lamers. A quantum lens on molecular design: A machine-learned energy function from interacting quantum atoms. *bioRxiv*, pages 2026–03, 2026.
- [17] Ross Irwin, Alessandro Tibo, Jon Paul Janet, and Simon Olsson. SemlaFlow—Efficient 3D molecular generation with latent attention and equivariant flow matching. *arXiv preprint arXiv:2406.07266*, 2024.

- [18] Kjell Jorner, Tore Brinck, Per-Ola Norrby, and David Buttar. Machine learning meets mechanistic modelling for accurate prediction of experimental activation energies. *Chemical Science*, 12(3):1163–1175, 2021.
- [19] Koichiro Kato, Tomohide Masuda, Chiduru Watanabe, Naoki Miyagawa, Hideo Mizouchi, Shumpei Nagase, Kikuko Kamisaka, Kanji Oshima, Satoshi Ono, Hiroshi Ueda, et al. High-precision atomic charge prediction for protein systems using fragment molecular orbital calculation and machine learning. *Journal of Chemical Information and Modeling*, 60(7):3361–3368, 2020.
- [20] Dávid Péter Kovács, J Harry Moore, Nicholas J Browning, Ilyes Batatia, Joshua T Horton, Yixuan Pu, Venkat Kapil, William C Witt, Ioan-Bogdan Magdau, Daniel J Cole, et al. Mace-off: Short-range transferable machine learning force fields for organic molecules. *Journal of the American Chemical Society*, 147(21):17598–17611, 2025.
- [21] Daniel S Levine, Muhammed Shuaibi, Evan Walter Clark Spotte-Smith, Michael G Taylor, Muhammad R Hasyim, Kyle Michel, Ilyes Batatia, Gábor Csányi, Misko Dzamba, Peter Eastman, et al. The Open Molecules 2025 (OMol25) dataset, evaluations, and models. *arXiv preprint arXiv:2505.08762*, 2025.
- [22] Sarah Lewis, Tim Hempel, José Jiménez-Luna, Michael Gastegger, Yu Xie, Andrew YK Foong, Víctor García Satorras, Osama Abdin, Bastiaan S Veeling, Iryna Zaporozhets, et al. Scalable emulation of protein equilibrium ensembles with generative deep learning. *Science*, 389(6761):eadv9817, 2025.
- [23] Shih-Cheng Li, Haoyang Wu, Angiras Menon, Kevin A Spiekermann, Yi-Pei Li, and William H Green. When do quantum mechanical descriptors help graph neural networks to predict chemical properties? *Journal of the American Chemical Society*, 146(33):23103–23120, 2024.
- [24] Chérif F Matta and Russell J Boyd. An introduction to the quantum theory of atoms in molecules. *The quantum theory of atoms in molecules*, 1, 2007.
- [25] Peter Maxwell, Nicodemo di Pasquale, Salvatore Cardamone, and Paul LA Popelier. The prediction of topologically partitioned intra-atomic and inter-atomic energies by the machine learning method kriging. *Theoretical Chemistry Accounts*, 135(8):195, 2016.
- [26] Leland McInnes, John Healy, Steve Astels, et al. hdbscan: Hierarchical density based clustering. *Journal of Open Source Software*, 2(11):205, 2017.
- [27] Derek P Metcalf, Andy Jiang, Steven A Spronk, Daniel L Cheney, and C David Sherrill. Electron-passing neural networks for atomic charge prediction in systems with arbitrary molecular charge. *Journal of Chemical Information and Modeling*, 61(1):115–122, 2020.
- [28] Brandon Meza-González, David I Ramírez-Palma, Pablo Carpio-Martínez, David Vázquez-Cuevas, Karina Martínez-Mayorga, and Fernando Cortés-Guzmán. Quantum topological atomic properties of 44k molecules. *Scientific Data*, 11(1):945, 2024.
- [29] Brandon Meza-González, David I. Ramírez-Palma, Pablo Carpio-Martínez, David Vázquez-Cuevas, Karina Martínez-Mayorga, and Fernando Cortés-Guzmán. Aimel-db: Atomic properties for 44k small organic molecules, February 2024. URL <https://doi.org/10.5281/zenodo.11406726>.
- [30] Robert G Parr and Weitao Yang. Density functional approach to the frontier-electron theory of chemical reactivity. *Journal of the American Chemical Society*, 106(14):4049–4050, 1984.
- [31] Saro Passaro, Gabriele Corso, Jeremy Wohlwend, Mateo Reveiz, Stephan Thaler, Vignesh Ram Somnath, Noah Getz, Tally Portnoi, Julien Roy, Hannes Stark, et al. Boltz-2: Towards accurate and efficient binding affinity prediction. *bioRxiv*, 2025.
- [32] Sergey Pozdnyakov and Michele Ceriotti. Smooth, exact rotational symmetrization for deep learning on point clouds. *Advances in Neural Information Processing Systems*, 36:79469–79501, 2023.
- [33] Raghunathan Ramakrishnan, Pavlo O Dral, Matthias Rupp, and O Anatole Von Lilienfeld. Quantum chemistry structures and properties of 134 kilo molecules. *Scientific Data*, 1(1):1–7, 2014.
- [34] Kristof Schütt, Oliver Unke, and Michael Gastegger. Equivariant message passing for the prediction of tensorial properties and molecular spectra. In *International Conference on Machine Learning*, pages 9377–9388. PMLR, 2021.
- [35] Peter Škrinjar, Jérôme Eberhardt, Janani Durairaj, and Torsten Schwede. Have protein-ligand co-folding methods moved beyond memorisation? *bioRxiv*, pages 2025–02, 2025.

- [36] Thijs Stuyver and Connor W Coley. Quantum chemistry-augmented neural networks for reactivity prediction: Performance, generalizability, and explainability. *The Journal of Chemical Physics*, 156(8), 2022.
- [37] Santiago Vargas, Winston Gee, and Anastassia Alexandrova. High-throughput quantum theory of atoms in molecules (QTAIM) for geometric deep learning of molecular and reaction properties. *Digital Discovery*, 3(5):987–998, 2024.
- [38] Max Veit, David M Wilkins, Yang Yang, Robert A DiStasio, and Michele Ceriotti. Predicting molecular dipole moments by combining atomic partial charges and atomic dipoles. *The Journal of chemical physics*, 153(2), 2020.
- [39] Jike Wang, Dongsheng Cao, Cunchen Tang, Lei Xu, Qiaojun He, Bo Yang, Xi Chen, Huiyong Sun, and Tingjun Hou. DeepAtomicCharge: A new graph convolutional network-based architecture for accurate prediction of atomic charges. *Briefings in Bioinformatics*, 22(3):bbaa183, 2021.
- [40] Claudio Zeni, Robert Pinsler, Daniel Zügner, Andrew Fowler, Matthew Horton, Xiang Fu, Zilong Wang, Aliaksandra Shysheya, Jonathan Crabbé, Shoko Ueda, et al. A generative model for inorganic materials design. *Nature*, 639(8055):624–632, 2025.

A Technical Appendices and Supplementary Material

A.1 Training and computational details

We report training and compute statistics for all models compared in this work in Table 3. We characterize per-batch compute using GFLOPs (giga floating-point operations, 10^9 FLOPs), measured as the cost of a single forward pass through the model on one training batch. EGFC model trained on A100fat GPU for about 2 days per fold. All other models trained on either A40 or A100 (based on GPU availability) and took from 12 to 36 hours per fold.

Table 3: Training and computational details for the models compared in Section 4. Parameter counts were chosen to keep model sizes approximately matched across architectures, while batch size and epoch count were tuned per model based on convergence behavior. Abbreviations: learning rate (LR); weight decay for AdamW (WD).

Models	# Params.	Batch Size	GFLOPs/Batch	Epochs	LR	WD
EGFC	486 786	128	17.88	1500	1.6e-3	1.2e-4
SFC2	686 081	256	20.30	2000	2.7e-3	1.6e-4
SGFC	487 598	128	8.67	3000	2.7e-3	1.6e-4
SG-8-12	686 049	256	9.25	2000	3.8e-3	1.1e-4
SG-8-5	686 049	2048	17.99	2000	3.8e-3	1.1e-4
EGNN	615 090	512	8.89	3000	3.8e-3	1.1e-4
SGNN	677 089	1024	8.96	3000	5.5e-3	9.1e-4

EGFC, EGNN, SGFC, and SGNN ran in a first round of experiments that used for loss function

$$\mathcal{L} = \frac{1}{N_{at}} \sum_{i=1}^{N_{at}} \frac{1}{4} \left[(\hat{N}_i - N_i)^2 + (\hat{\lambda}_i - \lambda_i)^2 + \frac{\sum_{\alpha=1}^3 (\hat{\mu}_i^{(\alpha)} - \mu_i^{(\alpha)})^2}{3} + \frac{\sum_{\alpha=1}^5 (\hat{Q}_i^{(\alpha)} - Q_i^{(\alpha)})^2}{5} \right],$$

where N_{at} is the total number of atoms in the training fold. For the rotationally augmented models, the training was slightly refined, adding per-element weights w_{Z_i} and modifying the quadrupole term to account for the Frobenius weights:

$$\mathcal{L} = \frac{1}{\sum_{i=1}^{N_{at}} w_{Z_i}} \sum_{i=1}^{N_{at}} \frac{w_{Z_i}}{4} \left[(\hat{N}_i - N_i)^2 + (\hat{\lambda}_i - \lambda_i)^2 + |\hat{\boldsymbol{\mu}}_i - \boldsymbol{\mu}_i|^2 + \|\hat{\mathbf{Q}}_i - \mathbf{Q}_i\|_F^2 \right].$$

The weight of each atom was normalized so that the sum of all atoms of a same element in the fold summed to 1, following $w_{Z_i} = \sqrt{N_{at}/N_{Z_i}}$.

For all models, the target quantities were z-score normalized, using mean and standard deviation for scalar properties and dividing by root mean square for tensor properties.

All points in the comparison stand, given the direct comparison between non-rotationally augmented and equivariant models in Section A.6.

A.2 Conventions

Our convention for representing a traceless tensor in Cartesian coordinates is

$$[T_{xx}, T_{xy}, T_{xz}, T_{yy}, T_{yz}, T_{zz}] \rightarrow [T_{xy}, T_{xz}, T_{yz}, T_{an}, T_{zz}],$$

where the anisotropic component is obtained from $T_{an} = \frac{T_{xx} - T_{yy}}{2}$. The equivariance-preserving Frobenius norm is therefore computed as

$$\|T\| = \sqrt{2(T_{xy}^2 + T_{xz}^2 + T_{yz}^2 + T_{an}^2) + \frac{3}{2}T_{zz}^2}. \quad (3)$$

A.3 Clustering of atomic environments

Element-specific HDBSCAN clustering parameters and resulting cluster counts are reported in Table 4, and the distributions of cluster labels across molecules in the dataset is shown in Figure 7.

Table 4: Element-specific details of HDBSCAN clustering. In all cases, we used the excess of mass method and no cluster merging.

	H	C	N	O
Number of atoms	278 943	199 660	30 805	40 894
PCA components	20	35	30	20
Variance retained (%)	99.11	99.01	99.18	99.04
Min. cluster size	850	850	100	100
Min. samples	200	200	30	30
Number of clusters	20	30	50	50
Noise points (%)	8.2	5.95	16.69	16.5

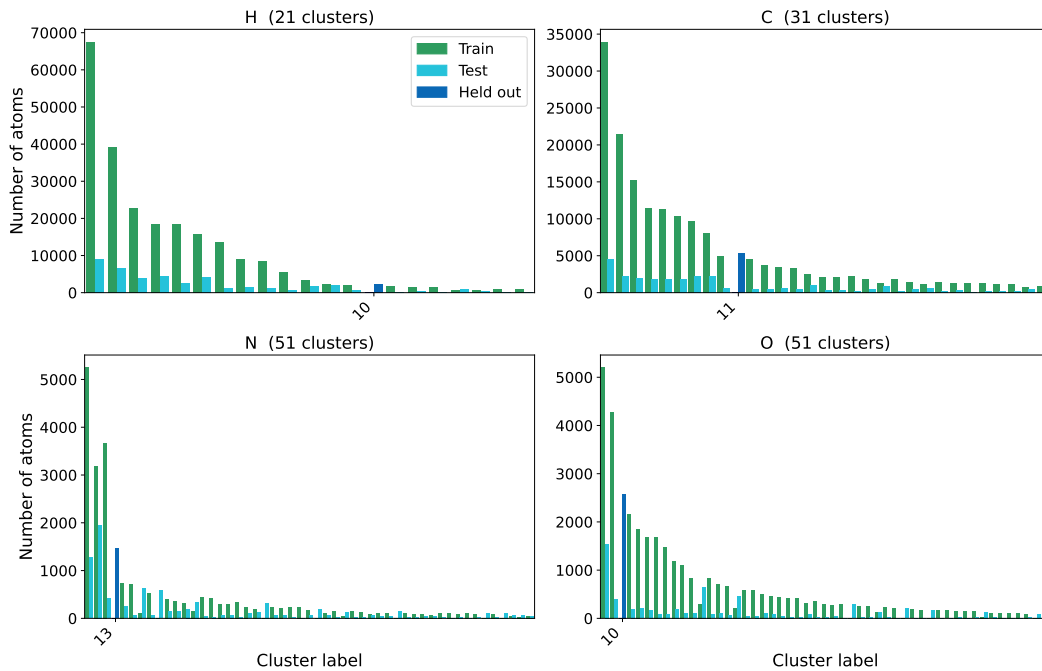


Figure 6: Number of atoms in each atomic environment. Only held out environment labels are included for clarity.

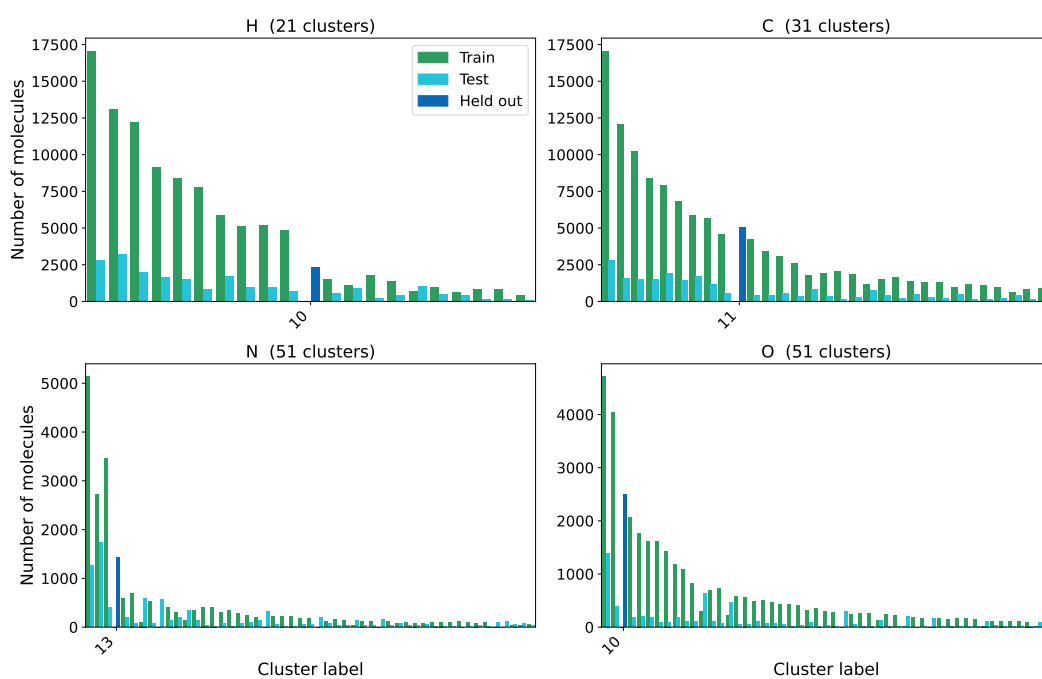


Figure 7: Number of molecules where an atomic environment occurs in the whole AIMED subset. Only held out environment labels are included for clarity.

A.4 Statistical validity of the model comparison

The statistical validity of the model comparison based on a fixed holdout design was assessed through three diagnostics computed exclusively over atoms carrying the held-out cluster labels H_10, C_11, N_13, and O_10 — enforcing the condition that no metric is diluted by environments seen during training (see text and Tabs. 5 and 6). Because the 5 repeat means reflect only training-sample variability (not holdout-selection variability), Tukey’s honest significant difference (HSD) error term is tighter than it would be under a random-holdout design. The resulting model rankings are statistically reliable for the defined OOD environments {H_10, C_11, N_13, O_10} and stable across training-set perturbations, as confirmed by the near-zero ICC. However, the confidence intervals do not capture uncertainty about the choice of holdout, so rankings should be interpreted as conditional on this specific evaluation set and not generalized to arbitrary OOD regimes.

Fold independence (ICC). The intraclass correlation ICC(1, 1) across the five inner folds within each repeat measures whether training-set composition variation causes correlated test performance within a repeat. All models returned near-zero or mildly negative ICC values when averaging over atoms and properties, indicating that folds contribute essentially independent information despite the partial overlap in training molecules. Negative values — observed in several strata of the SI table (Tab. 7) — arise naturally when training-set variability is dominated by which environments are *excluded* rather than included, and do not indicate a violation. The effective sample size $n_{\text{eff}} \in [16.5, 25.0]$ across models reflects this near-independence and confirms that the standard repeated-CV estimator remains close to unbiased.

Normality and homoscedasticity (SW and Levene). Shapiro–Wilk normality tests on the five repeat-level means passed for 87.5–100% when averaging over atoms and properties, only descending below 75% when looking at per-atom type scores. Levene homoscedasticity tests passed for 93.8% when scores were averaged over property and atom label, only descending to 75% for certain atom types. Together, these diagnostics confirm that the RM-ANOVA and Tukey HSD assumptions are met in practice for CCC.

Table 5: ANOVA validity diagnostics for averaged CCC metrics of rotationally augmented and equivariant models. All quantities computed exclusively over atoms carrying held-out cluster label. **ICC**(1, 1): intraclass correlation across the five inner folds within each repeat; ideal range $[-0.10, 0.10]$ (near-independent folds, $n_{\text{eff}} \approx 25$); orange if $|\text{ICC}| > 0.20$, red if > 0.40 . n_{eff} : effective sample size = $25 / (1 + (k - 1) \cdot \max(0, \text{ICC}))$; orange if $< 80\%$ of nominal (< 20), red if $< 60\%$ (< 15). **SW**: Shapiro–Wilk pass rate (%) on five repeat-means; orange if $< 80\%$, red if $< 60\%$. **Lev.**: Levene homoscedasticity pass rate (%) across models; same thresholds.

Diagnostic	EGNN	SG-8-5	SG-8-12	SFC2	EGFC
ICC(1, 1)	0.008 ± 0.097	0.043 ± 0.137	-0.006 ± 0.126	0.008 ± 0.140	-0.050 ± 0.138
n_{eff}	22.3 ± 3.7	20.2 ± 4.7	22.0 ± 4.4	21.5 ± 4.5	22.7 ± 4.0
SW	100.0	87.5	81.2	100.0	100.0
Lev.	93.8	93.8	93.8	93.8	93.8

Table 6: ANOVA validity diagnostics for averaged CCC metrics of non-augmented. All quantities computed exclusively over atoms carrying held-out cluster label. **ICC**(1, 1): intraclass correlation across the five inner folds within each repeat; ideal range $[-0.10, 0.10]$ (near-independent folds, $n_{\text{eff}} \approx 25$); orange if $|\text{ICC}| > 0.20$, red if > 0.40 . n_{eff} : effective sample size = $25 / (1 + (k - 1) \cdot \max(0, \text{ICC}))$; orange if $< 80\%$ of nominal (< 20), red if $< 60\%$ (< 15). **SW**: Shapiro–Wilk pass rate (%) on five repeat-means; orange if $< 80\%$, red if $< 60\%$. **Lev.**: Levene homoscedasticity pass rate (%) across models; same thresholds.

Diagnostic	SGNN	SGFC
ICC(1, 1)	-0.035 ± 0.129	-0.116 ± 0.064
n_{eff}	18.0 ± 3.6	24.8 ± 0.7
SW	93.8	93.8
Lev.	100.0	100.0

Table 7: Full ANOVA validity diagnostics of the models in the main discussion per held-out label and property. All quantities computed exclusively over atoms carrying held-out cluster label. $\text{ICC}(1,1)$: intraclass correlation across the five inner folds within each repeat; ideal range $[-0.10, 0.10]$ (near-independent folds, $n_{\text{eff}} \approx 25$); orange if $|\text{ICC}| > 0.20$, red if > 0.40 . n_{eff} : effective sample size $= 25 / (1 + (k - 1) \cdot \max(0, \text{ICC}))$; orange if $< 80\%$ of nominal (< 20), red if $< 60\%$ (< 15). **SW**: Shapiro–Wilk pass rate (%) on five repeat-means; orange if $< 80\%$, red if $< 60\%$. **Lev**: Levene homoscedasticity pass rate (%) across models; same thresholds.

Model	Property	H_10			C_11			N_13			O_10						
		ICC(1,1)	n_{eff}	SW	Lev.	ICC(1,1)	n_{eff}	SW	Lev.	ICC(1,1)	n_{eff}	SW	Lev.	ICC(1,1)	n_{eff}	SW	Lev.
EGNN	N	-0.037	25.0	100.0	100.0	-0.025	25.0	100.0	100.0	-0.100	25.0	100.0	100.0	0.153	15.5	100.0	100.0
	λ	0.076	19.2	100.0	100.0	0.020	23.1	100.0	100.0	-0.205	25.0	100.0	100.0	0.209	13.6	100.0	0.0
	$ \mu $	-0.019	25.0	100.0	100.0	-0.016	25.0	100.0	100.0	-0.036	25.0	100.0	100.0	0.111	17.3	100.0	100.0
	$ \mathbf{Q} $	0.001	24.9	100.0	100.0	0.042	21.4	100.0	100.0	-0.081	25.0	100.0	100.0	0.035	21.9	100.0	100.0
SG-8-5	N	-0.071	25.0	100.0	100.0	0.070	19.5	100.0	100.0	0.082	18.8	100.0	100.0	-0.017	25.0	100.0	100.0
	λ	-0.149	25.0	100.0	100.0	0.092	18.3	100.0	100.0	-0.132	25.0	100.0	100.0	0.129	16.5	0.0	0.0
	$ \mu $	-0.065	25.0	100.0	100.0	0.102	17.7	100.0	100.0	0.019	23.2	100.0	100.0	0.343	10.5	100.0	100.0
	$ \mathbf{Q} $	-0.177	25.0	100.0	100.0	0.061	20.1	0.0	100.0	0.201	13.8	100.0	100.0	0.199	13.9	100.0	100.0
SG-8-12	N	0.049	20.9	100.0	100.0	-0.011	25.0	100.0	100.0	-0.143	25.0	100.0	100.0	-0.165	25.0	100.0	100.0
	λ	0.213	13.5	100.0	100.0	-0.100	25.0	100.0	100.0	-0.066	25.0	100.0	100.0	-0.196	25.0	0.0	0.0
	$ \mu $	0.146	15.8	100.0	100.0	0.045	21.2	100.0	100.0	0.079	19.0	100.0	100.0	0.255	12.4	100.0	100.0
	$ \mathbf{Q} $	-0.073	25.0	100.0	100.0	0.002	24.9	0.0	100.0	-0.055	25.0	100.0	100.0	-0.068	25.0	0.0	100.0
SFC2	N	0.011	24.0	100.0	100.0	-0.098	25.0	100.0	100.0	0.143	15.9	100.0	100.0	-0.042	25.0	100.0	100.0
	λ	0.072	19.4	100.0	100.0	0.001	24.9	100.0	100.0	0.348	10.5	100.0	100.0	0.025	22.7	100.0	0.0
	$ \mu $	0.157	15.3	100.0	100.0	-0.160	25.0	100.0	100.0	0.069	19.6	100.0	100.0	0.124	16.7	100.0	100.0
	$ \mathbf{Q} $	-0.193	25.0	100.0	100.0	-0.109	25.0	100.0	100.0	-0.043	25.0	100.0	100.0	-0.181	25.0	100.0	100.0
EGFC	N	-0.104	25.0	100.0	100.0	0.007	24.3	100.0	100.0	-0.127	25.0	100.0	100.0	0.050	20.8	100.0	100.0
	λ	-0.097	25.0	100.0	100.0	0.149	15.7	100.0	100.0	-0.208	25.0	100.0	100.0	-0.090	25.0	100.0	0.0
	$ \mu $	-0.178	25.0	100.0	100.0	-0.178	25.0	100.0	100.0	0.093	18.2	100.0	100.0	0.017	23.4	100.0	100.0
	$ \mathbf{Q} $	-0.195	25.0	100.0	100.0	0.299	11.4	100.0	100.0	-0.154	25.0	100.0	100.0	-0.086	25.0	100.0	100.0

A.5 Additional plots and metrics for the discussion on predicting QTA properties

We include here numerical values of CCC (Tab. 8) and Tukey forest plots for the equivariant and rotationally augmented models (Fig. 8). Per-element and per-property differences must be interpreted keeping in mind that the statistical validity gets compromised at this stratum (see Tab. 7). It is worth noticing that, when accounting for all atoms in the test set, all models achieve CCC > 0.9 in all properties and atoms (Fig. 9).

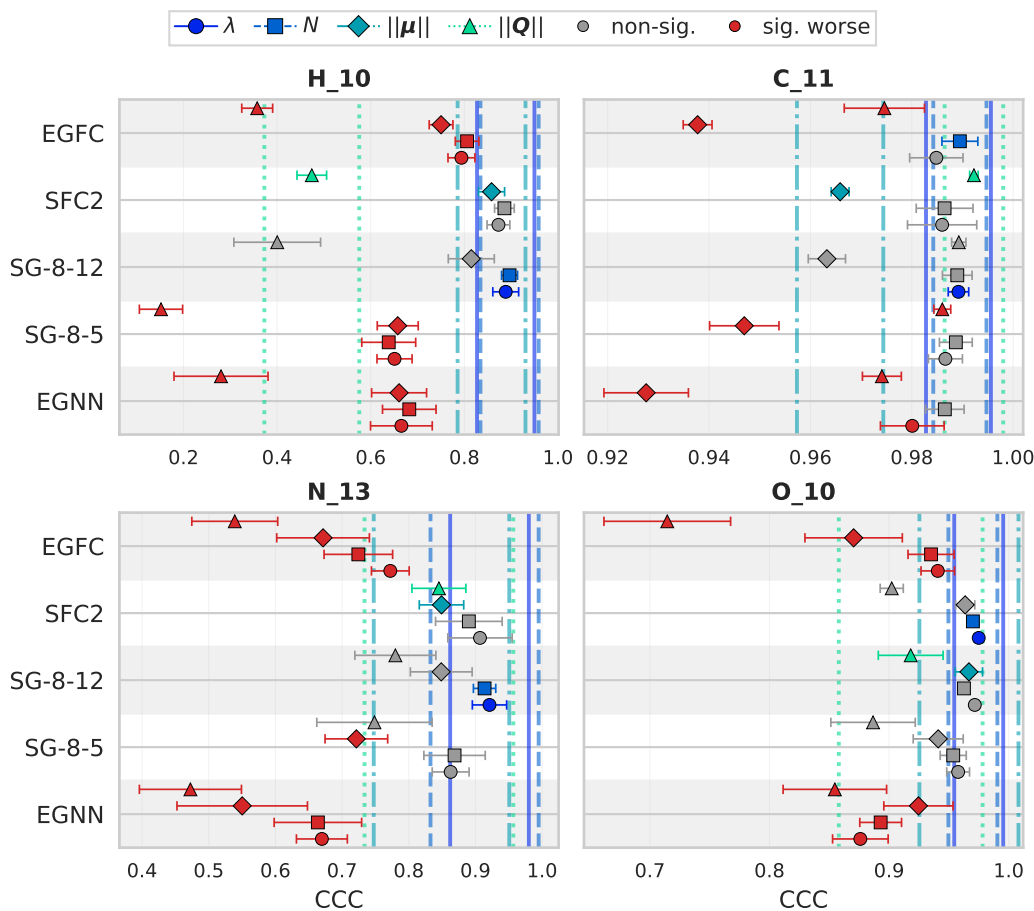


Figure 8: Tukey forest plots for CCC scores of each model, for each atom and property in the holdout set. The best performing model for each (atom, property) shows a coloured symbol surrounded by the minimum significant difference.

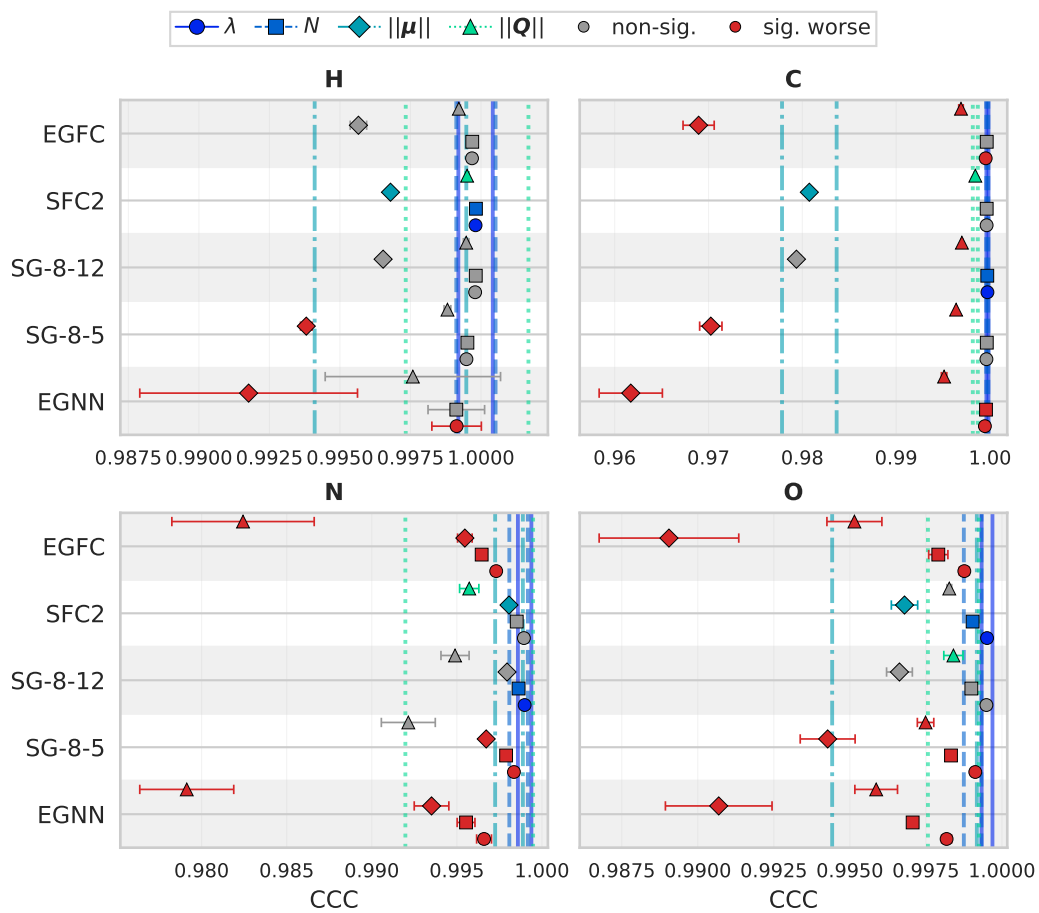


Figure 9: Tukey forest plots for CCC scores of each model, for each atom and property for all of the test set. The best performing model for each (atom, property) shows a coloured symbol surrounded by the minimum significant difference.

Table 8: Model comparison on CCC (mean \pm 95 % CI over $n = 5$ CV repeats). Cell colour: 1st 2nd 3rd per row.

Cluster	Property	EGNN	SG-8-5	SG-8-12	SFC2	EGFC
H_10	N	0.682 ± 0.057	0.638 ± 0.058	0.897 ± 0.017	0.886 ± 0.021	0.806 ± 0.025
	λ	0.665 ± 0.066	0.651 ± 0.037	0.888 ± 0.028	0.873 ± 0.024	0.794 ± 0.029
	$ \mu $	0.661 ± 0.059	0.658 ± 0.044	0.815 ± 0.049	0.858 ± 0.028	0.750 ± 0.025
	$ \mathbf{Q} $	0.280 ± 0.100	0.152 ± 0.046	0.400 ± 0.093	0.474 ± 0.032	0.357 ± 0.033
C_11	N	0.987 ± 0.004	0.989 ± 0.003	0.989 ± 0.003	0.986 ± 0.006	0.989 ± 0.004
	λ	0.980 ± 0.006	0.987 ± 0.003	0.989 ± 0.002	0.986 ± 0.007	0.985 ± 0.005
	$ \mu $	0.928 ± 0.008	0.947 ± 0.007	0.963 ± 0.004	0.966 ± 0.002	0.938 ± 0.003
	$ \mathbf{Q} $	0.974 ± 0.004	0.986 ± 0.002	0.989 ± 0.001	0.992 ± 0.001	0.975 ± 0.008
N_13	N	0.664 ± 0.066	0.869 ± 0.046	0.914 ± 0.017	0.890 ± 0.050	0.724 ± 0.051
	λ	0.670 ± 0.038	0.863 ± 0.028	0.921 ± 0.026	0.907 ± 0.048	0.772 ± 0.028
	$ \mu $	0.550 ± 0.098	0.721 ± 0.047	0.849 ± 0.046	0.849 ± 0.033	0.671 ± 0.069
	$ \mathbf{Q} $	0.473 ± 0.077	0.749 ± 0.086	0.780 ± 0.061	0.845 ± 0.040	0.539 ± 0.064
O_10	N	0.893 ± 0.017	0.954 ± 0.011	0.963 ± 0.003	0.970 ± 0.005	0.935 ± 0.019
	λ	0.876 ± 0.023	0.958 ± 0.010	0.972 ± 0.002	0.975 ± 0.004	0.941 ± 0.014
	$ \mu $	0.925 ± 0.029	0.941 ± 0.021	0.967 ± 0.011	0.964 ± 0.008	0.870 ± 0.041
	$ \mathbf{Q} $	0.855 ± 0.043	0.887 ± 0.035	0.918 ± 0.027	0.902 ± 0.010	0.715 ± 0.053

A.6 Additional discussion on the effect of layer depth

Here, we provide arguments in favor that the greater depth of the scalar models is not being invested in passing chemical information, but rather in polishing the purely geometrical information that equivariant models understand by design. To confirm this, we trained two non-augmented, scalar GNNs matching the connectivity of EGNN and EGFC. We refer to these two non-augmented models as SGNN and SGFC. In Figure 10, we include radial distributions for reference.

The results in Tab. 9 show that the difference between EGNN and SGNN is not significant. Therefore, at equal connectivity and without data augmentation, the greater depth is being invested in geometric learning. The significant performance difference between SGFC and EGFC suggests that the geometric understanding of non-equivariant models can highly benefit from a denser connectivity.

Table 9: Tukey p-value matrix of CCC scores averaged over atom types and properties, comparing non-data augmented, non-equivariant models with equivariant models. A value below 0.05 indicates a statistically significant difference in performance. The best performing models are determined based on CCC mean value and statistical significance of the difference: **1st** **2nd** **3rd**.

Models	Tukey p-values				CCC \pm 95% CI
	EGFC	SGFC	EGNN	SGNN	
EGFC	1.0000	0.0010	0.0010	0.0010	0.798 \pm 0.006
SGFC	0.0010	1.0000	0.0010	0.0010	0.844 \pm 0.011
EGNN	0.0010	0.0010	1.0000	0.6128	0.754 \pm 0.028
SGNN	0.0010	0.0010	0.6128	1.0000	0.744 \pm 0.018

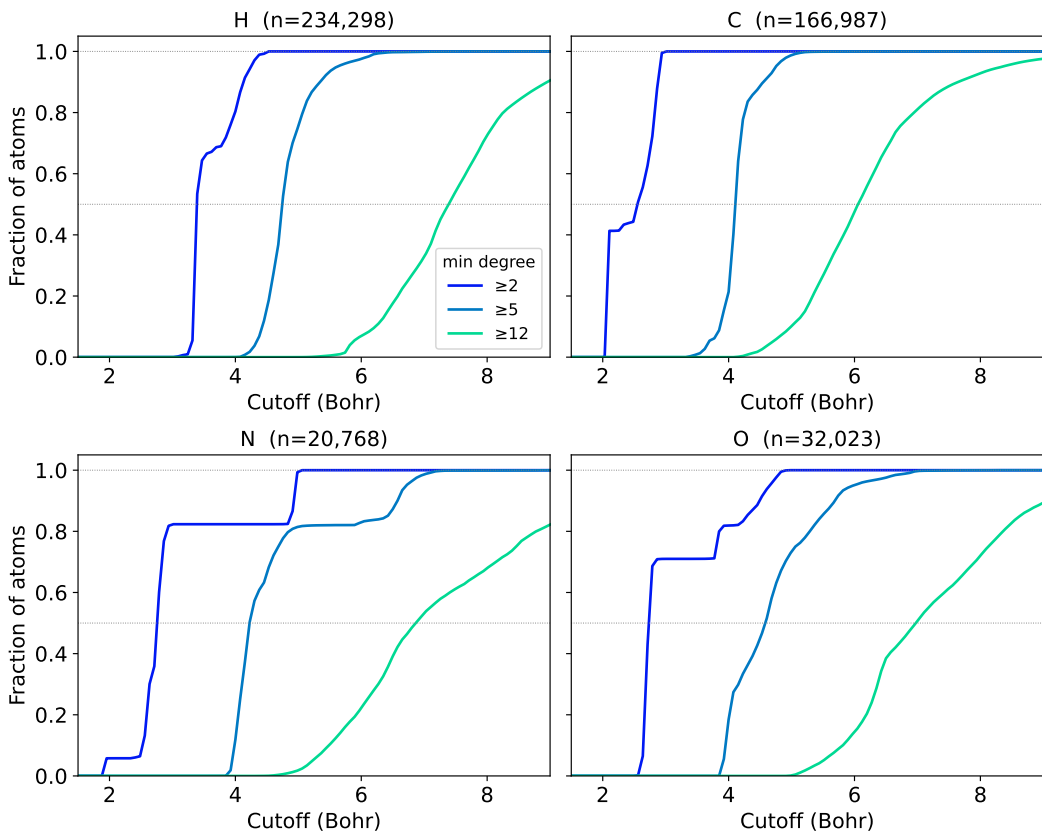


Figure 10: Distributions of fractions of atoms in training by minimum number of neighbors at each cutoff.

A.7 Molecular property prediction experiments

The informed and blind models are evaluated on the same 5×5 cross-validation folds, so each (informed, blind) pair is matched on identical training/test splits. This pairing motivates a two-sided paired test on the 25 fold-level R^2 differences $\Delta_i = R_{\text{informed},i}^2 - R_{\text{blind},i}^2$, performed independently for every (training fraction, property) cell. Table 10 reports the mean difference ΔR^2 together with its standard error of the mean ($\text{SEM} = \text{std}(\Delta)/\sqrt{n}$, $n = 25$), so positive values indicate advantage of informed models and the SEM quantifies the uncertainty on ΔR^2 itself rather than the spread of Δ_i . Two complementary tests are reported, each with its assumptions verified in the same table. The paired t -test requires independence and approximate normality of Δ_i , checked respectively in the "ICC (Δ)" and "SW (Δ) p " columns; the Wilcoxon signed-rank test requires independence and symmetry of Δ_i — independence shares the ICC column, while symmetry is not tested directly but is supported by the consistent agreement between the two tests across all sixteen cells (see below). Independence is satisfied throughout ($\max |\text{ICC}| = 0.18$, comfortably below the 0.20 caution threshold), so the two tests differ only in their distributional assumption (normality vs. symmetry), giving the analysis a built-in fallback whenever $\text{SW}(\Delta)$ is small.

Seven of the sixteen cells satisfy $\text{SW}(\Delta) \geq 0.05$ and the paired- t test is valid by assumption. The remaining nine cells reject normality at $\alpha = 0.05$; however, in every such cell the Wilcoxon and paired- t agree on the same conclusion (significant or non-significant), so the overall pattern is invariant to the choice of test. The mean differences ΔR^2 are positive and significantly above zero (i.e. informed models significantly outperform blind counterparts) for α , U_0 , and C_v at every training fraction, and for the HOMO–LUMO gap at the full training set (1.0); the only non-significant cells are gap at low fractions and U_0 at fraction 1.0, where both models reach $R^2 \approx 0.997$ and a real but vanishing ΔR^2 cannot be resolved with $n = 25$ folds.

Table 10: Statistical validity metrics for the comparison of blind and informed models on the AIMEL subset for R^2 on $n = 25$ folds. $\Delta R^2 \pm \text{SEM}$: fold-wise mean of $\Delta_i = R_{\text{Inf},i}^2 - R_{\text{Blind},i}^2$ with standard error of that mean ($\text{SEM} = \text{std}(\Delta)/\sqrt{n}$). Positive values favour informed models. **ICC (Δ)**: one-way ICC(1,1) of the 25 fold-level differences grouped by the 5 outer repeats; if near zero, folds carry independent information across repeats. Shaded orange for $|\text{ICC}| \geq 0.20$ and red for $|\text{ICC}| \geq 0.40$. **SW (Δ) p** : Shapiro–Wilk on the 25 paired differences. **paired- t p** , **Wilcoxon p** : two-sided p -values for the null hypothesis of zero mean informed–blind performance difference. Cells shaded red when $p < \alpha = 0.05$ and orange when $\alpha \leq p < 10\alpha$.

Fraction	Quantity	α	$\Delta\varepsilon$	U_0	C_v
0.01	$\Delta R^2 \pm \text{SEM}$	0.055±0.020	-0.020±0.013	0.087±0.022	0.067±0.018
	ICC (Δ)	-0.112	-0.151	-0.134	-0.076
	SW (Δ) p	0.388	0.138	0.205	0.494
	paired- t p	0.011	0.140	0.001	0.001
	Wilcoxon p	0.014	0.300	0.001	0.001
0.05	$\Delta R^2 \pm \text{SEM}$	0.013±0.004	0.003±0.002	0.018±0.004	0.021±0.003
	ICC (Δ)	-0.109	-0.138	-0.044	-0.023
	SW (Δ) p	0.000	0.513	0.000	0.000
	paired- t p	0.001	0.186	0.001	0.000
	Wilcoxon p	0.000	0.173	0.000	0.000
0.1	$\Delta R^2 \pm \text{SEM}$	0.005±0.001	-0.001±0.002	0.003±0.001	0.018±0.002
	ICC (Δ)	-0.076	-0.146	0.015	-0.178
	SW (Δ) p	0.000	0.001	0.002	0.001
	paired- t p	0.000	0.505	0.002	0.000
	Wilcoxon p	0.001	0.979	0.001	0.000
1.0	$\Delta R^2 \pm \text{SEM}$	0.003±0.000	0.013±0.001	0.000±0.000	0.010±0.001
	ICC (Δ)	-0.059	-0.016	-0.010	0.004
	SW (Δ) p	0.030	0.926	0.624	0.002
	paired- t p	0.000	0.000	0.163	0.000
	Wilcoxon p	0.000	0.000	0.127	0.000

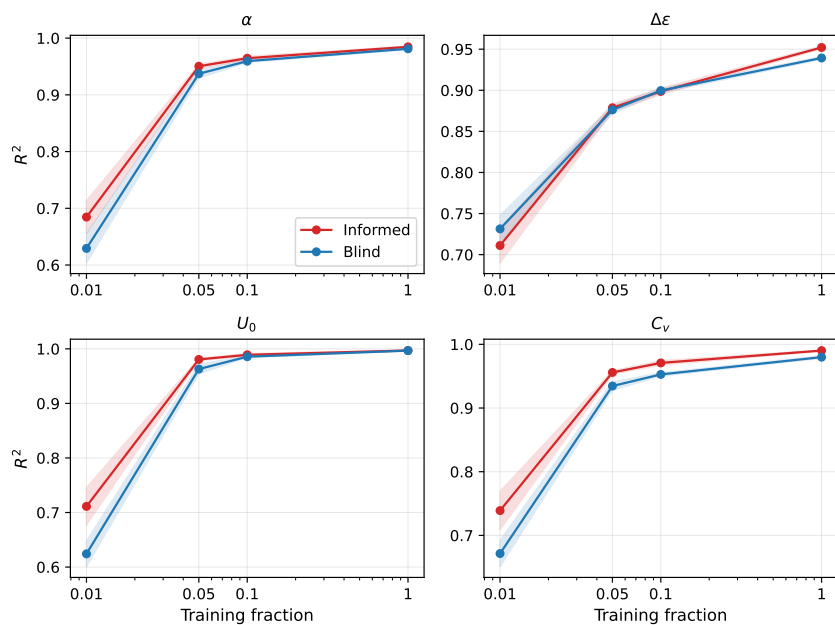


Figure 11: Value of R^2 of predictions on AIMEl molecules for each property (α , $\Delta\epsilon$, U_0 , C_v) at each training fraction.

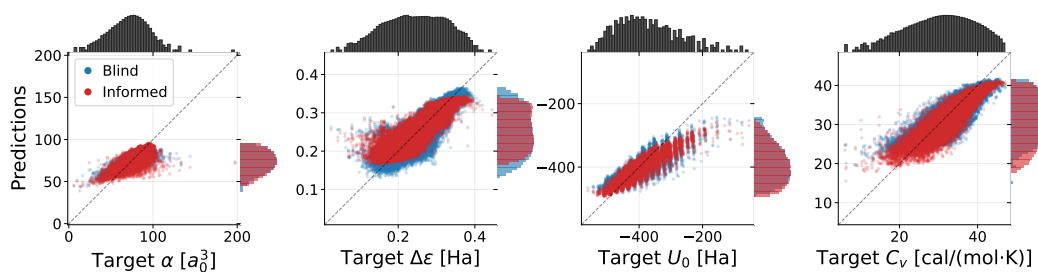


Figure 12: Parity plots for ensemble predictions of informed and blind models trained on 0.01 fraction of the data in AIMEl, when deployed on the remainder of QM9.

A.8 Equivariant models

In the following, we use L to denote the label of the irreducible representation (irrep) of $SO(3)$ with dimension $2L + 1$. We represent each atom by a node with scalar features h_i , vector features \mathbf{x}_i and traceless, symmetric features \mathbf{T}_i . For edge features, we follow the same convention, but with double subindexes (e.g., h_{ij}). We denote the channel-wise (Hadamard) product with \odot and the outer product with \otimes . We refer to the whole array of features by $f \equiv (h, \mathbf{x}, \mathbf{T})$, and to the $L > 0$ (non-scalar) features by $\mathbf{f} \equiv (\mathbf{x}, \mathbf{T})$. We refer to the concatenation of invariants by $\|f\| \equiv (h, \|\mathbf{x}\|, \|\mathbf{T}\|)$. Throughout the models, we apply normalization separately to each irreducible representation: LayerNorm for scalar features and the equivariant E3Norm of Batatia et al. [4] for vector and tensor features. We denote normalized features uniformly by $\tilde{f} = \text{E3Norm}(f)$, with the understanding that E3Norm reduces to LayerNorm for the scalar case. For non-scalar features,

$$\tilde{\mathbf{f}}_{i,c} = w_c \cdot \frac{\mathbf{f}_{i,c}}{\sqrt{\|\mathbf{f}_{i,c}\|^2 + \varepsilon}},$$

where i is the cell (atom) index, c indexes the parallel feature channels within a given irrep, w_c is a learnable per-channel scaling weight, and ε is a small constant for numerical stability. Because the normalization acts only on the magnitude of $\mathbf{f}_{i,c}$ and not on its components individually, the orientation of each vector or tensor feature is preserved — which is what allows E3Norm to be used inside an equivariant architecture without breaking the equivariance.

In all models, node features are initialized with a message passing layer as follows:

$$h_i^{(0)} = \text{LayerNorm} \left(\sum_j m_{ij}^s \odot \Gamma_0^s(r_{ij}) \right) \quad (4)$$

$$\mathbf{x}_i^{(0)} = \text{E3Norm} \left(\sum_j m_{ij}^v \odot \Gamma_0^v(r_{ij}) \otimes \hat{\mathbf{r}}_{ij} \right) \quad (5)$$

$$\mathbf{T}_i^{(0)} = \text{E3Norm} \left(\sum_j m_{ij}^t \odot \Gamma_0^t(r_{ij}) \otimes \hat{\mathbf{G}}_{ij} \right) \quad (6)$$

where the messages m_{ij} are generated by a multi-layer perceptron (MLP) that takes as input the embeddings of the atomic species, $m_{ij} = \text{MLP}(\text{EMBED}(Z_i), \text{EMBED}(Z_j))$, and $\Gamma_L^s, \Gamma_L^v, \Gamma_L^t$ are geometric filters that map a projection of the inter-atomic displacement onto a radial basis functions, and output channel-wise sigmoid gates. Finally, $\hat{\mathbf{G}}_{ij} \propto \hat{\mathbf{r}}_{ij} \otimes \hat{\mathbf{r}}_{ij}$ is the unit-norm outer product of the relative position vector, expressed in the traceless symmetric representation as

$$\hat{\mathbf{G}}(\hat{\mathbf{r}}) = \sqrt{3/2} [r_x r_y, r_x r_z, r_y r_z, (r_x^2 - r_y^2)/2, r_z^2 - 1/3] \equiv [G_{xy}, G_{xz}, G_{yz}, G_{an}, G_{zz}].$$

The unit norm follows from the Frobenius norm in Eq. 3.

Edge features are initialized from these node features as follows

$$h_{ij}^{(0)} = \text{LayerNorm} \left(\Psi^s \left(\text{LayerNorm} \left(\sum_{k \in \{i,j\}} \psi^s(\|f_k^{(0)}\|) \right) \right) \odot \Gamma_1^s(r_{ij}) \right) \quad (7)$$

$$\mathbf{x}_{ij}^{(0)} = \text{E3Norm} \left(\left(\sum_{k \in \{i,j\}} \psi^v(\|f_k^{(0)}\|) \odot (W^v \mathbf{x}_k^{(0)}) \right) \odot \Gamma_1^v(r_{ij}) \right) \quad (8)$$

$$\mathbf{T}_{ij}^{(0)} = \text{E3Norm} \left(\left(\sum_{k \in \{i,j\}} \psi^t(\|f_k^{(0)}\|) \odot (W^t \mathbf{T}_k^{(0)}) \right) \odot \Gamma_1^t(r_{ij}) \right) \quad (9)$$

where the superscripts s , v , and t denote separate parameter sets for the scalar, vector, and tensor channels respectively; Ψ and ψ are MLPs acting on per-node feature norms; and W^v and W^t are

learnable linear maps between node and edge channel dimensions (taken as the identity when these dimensions match)

After these, all layers follow a residual update structure, $f'_r = f_r + g(\|f_r\|) \odot M_r(\tilde{f}_r, \tilde{f}_s, \tilde{f}_t)$, where g is a gating MLP with a sigmoid output that depends on the unnormed features, and $M_r(\tilde{f}_r, \tilde{f}_s, \tilde{f}_t)$ is a message aggregation with $\tilde{f}_r, \tilde{f}_s, \tilde{f}_t$ being E3Normed receiver, sender, and intermediary features, respectively. In general,

$$M_r(\tilde{f}_r, \tilde{f}_s, \tilde{f}_t) = \sum_{s,t \in \mathcal{N}_i(r)} m(\tilde{f}_r, \tilde{f}_s, \tilde{f}_t) \odot \Gamma(\mathbf{R}_r, \mathbf{R}_s) \odot W \tilde{f}_s, \quad (10)$$

where W is a linear map to match dimensions (if necessary), and the message generating function is an MLP

$$m(\tilde{f}_r, \tilde{f}_s, \tilde{f}_t) = \text{MLP}\left(\tilde{h}_r, \tilde{h}_s, \|U\tilde{\mathbf{f}}_r\|, \|V\tilde{\mathbf{f}}_s\|, \cos(U\tilde{\mathbf{f}}_r, V\tilde{\mathbf{f}}_s), \|\tilde{f}_t\|\right), \quad (11)$$

with U and V being linear maps applied to the $L > 0$ channels, and $\cos(A, B)$ being the cosine similarity of the $L > 0$ channels. This way, the messages are generated based on both magnitude and directional information.

The geometric filter Γ takes as input an invariant geometric relation between the receiver and sender real-space geometric information, $\mathbf{R}_r, \mathbf{R}_s$, and is absent in layers where there is no obvious geometric relation or to avoid redundant information from previous transformations (e.g., edge-to-node messages in late layers). In node-to-node and node-to-edge messages, we use radial basis functions evaluated at the length of the edge (i.e. distance between node and receiver nodes). In edge-to-edge messages, we project $\cos(\mathbf{G}_r, \mathbf{G}_s) = \text{Tr}(\hat{\mathbf{G}}_r^T \hat{\mathbf{G}}_s)$ onto a basis of Legendre polynomials, $\{P_n(x)\}$, since the gyration tensors contain angular information.

At certain steps, geometry is re-injected to avoid degradation of geometric signal. In this case, the residual connection gets two simultaneous updates, one for features and one for geometry,

$$f'_r = f_r + g_f(\|f_r\|) \odot M_r + g_{\mathbf{R}}(\|f_r\|) \odot \Delta \mathbf{f}_r, \quad (12)$$

where

$$\Delta \mathbf{f}_r = \sum_{s,t \in \mathcal{N}_i(r)} m(\tilde{f}_r, \tilde{f}_s, \tilde{f}_t) \odot \Gamma(\mathbf{R}_r, \mathbf{R}_s) \odot \Delta \hat{\mathbf{R}}_{rs}. \quad (13)$$

Here, $\Delta \hat{\mathbf{R}}_{rs} = (\hat{\mathbf{r}}_{rs}, \hat{\mathbf{G}}_{rs})$ is a unit-norm tensor.

At the end of a messaging cycle, we apply a feed-forward residual update following the expression

$$f'_r = f_r + g(\|f_r\|) \odot \text{MLP}(\|f_r\|, W \cdot \text{EMBED}(Z_r)) \odot (\mathbb{I}_0 | \tilde{\mathbf{f}}_r) \quad (14)$$

where \mathbb{I}_0 is the identity over the scalar channels (i.e. scalar features are not gated). We include a linear transformation of the initial embedding of the atomic species whenever this layer is applied to nodes, but that term is omitted when applied to edges.

Finally, the prediction of the model for the properties of a given atom, $\hat{y}_i = (\hat{N}_i, \hat{\lambda}_i, \hat{\mu}_i, \hat{\mathbf{Q}}_i)$ is a readout that depends on an atomic head at the end of each layer:

$$(\hat{N}_i^{(l)}, \hat{\lambda}_i^{(l)}) = \text{MLP}(h_i^{(l)}), \quad \hat{\mu}_i^{(l)} = \sum_c w_c^{v,(l)} \mathbf{x}_{i,c}^{(l)}, \quad \hat{\mathbf{Q}}_i^{(l)} = \sum_c w_c^{t,(l)} \mathbf{T}_{i,c}^{(l)},$$

$$\text{and } \hat{y}_i = \sum_l \alpha^{(l)} \hat{y}_i^{(l)},$$

where the layer weights α come from a softmax, $\alpha^{(l)} = \exp(\omega^{(l)}) / \sum_{l'} \exp(\omega^{(l')})$.

A.9 Parity plots for the OOD predictions of QT-Net on AIMEL

We show parity plots for QT-Net’s predictions on the held-out atomic environments $\{\text{H}_{10}, \text{C}_{11}, \text{N}_{13}, \text{O}_{10}\}$ for each of the four QTA targets: electron populations N (Fig. 13), localization indices λ (Fig. 14), atomic contributions to the molecular dipole moment μ (Fig. 15), and quadrupole moments \mathbf{Q} (Fig. 16).

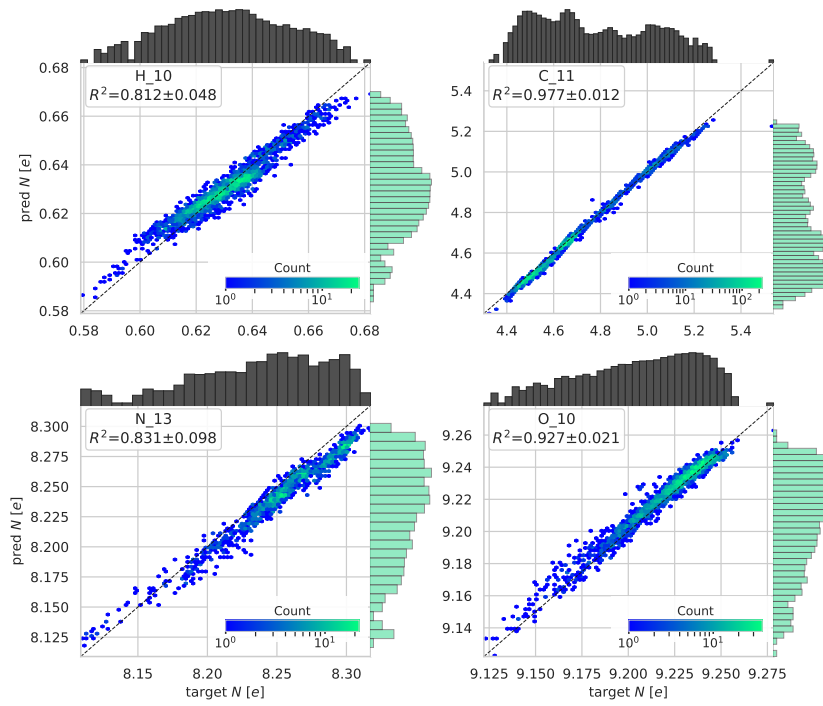


Figure 13: Parity plot for the OOD predictions of QT-Net for electron populations.

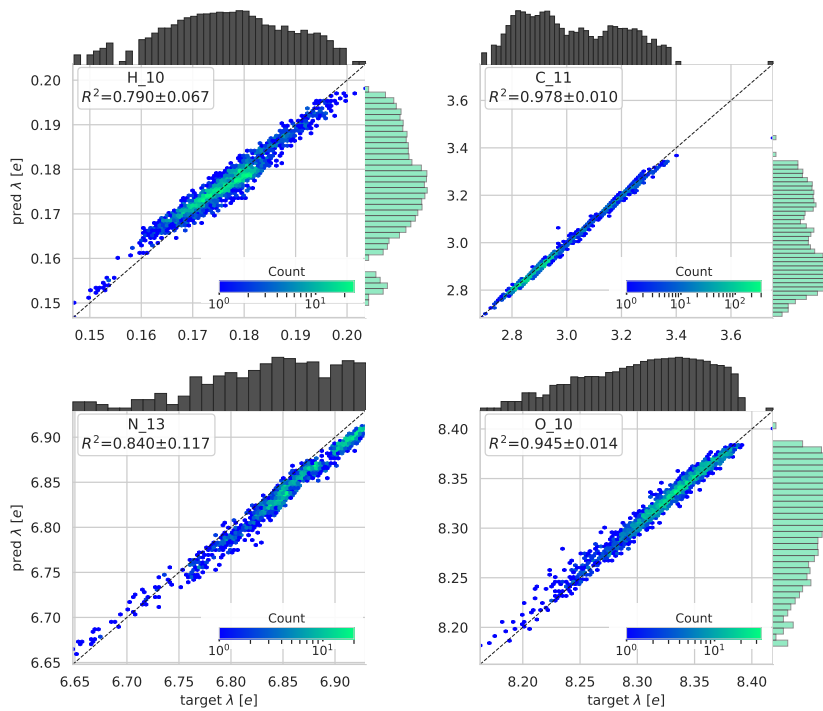


Figure 14: Parity plot for the OOD predictions of QT-Net for localization indices.

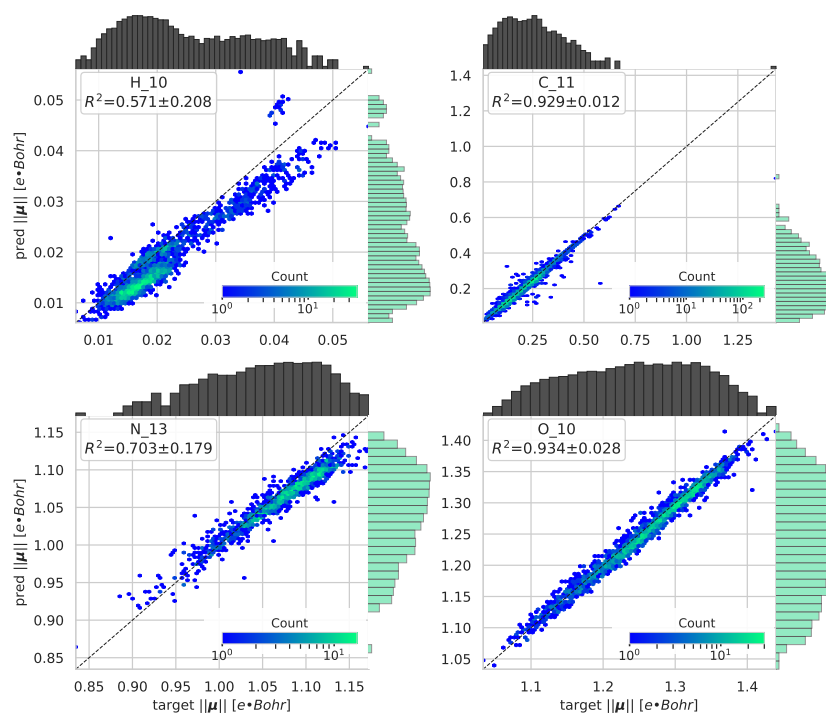


Figure 15: Parity plot for the OOD predictions of QT-Net for atomic contributions to the molecular dipole moment.

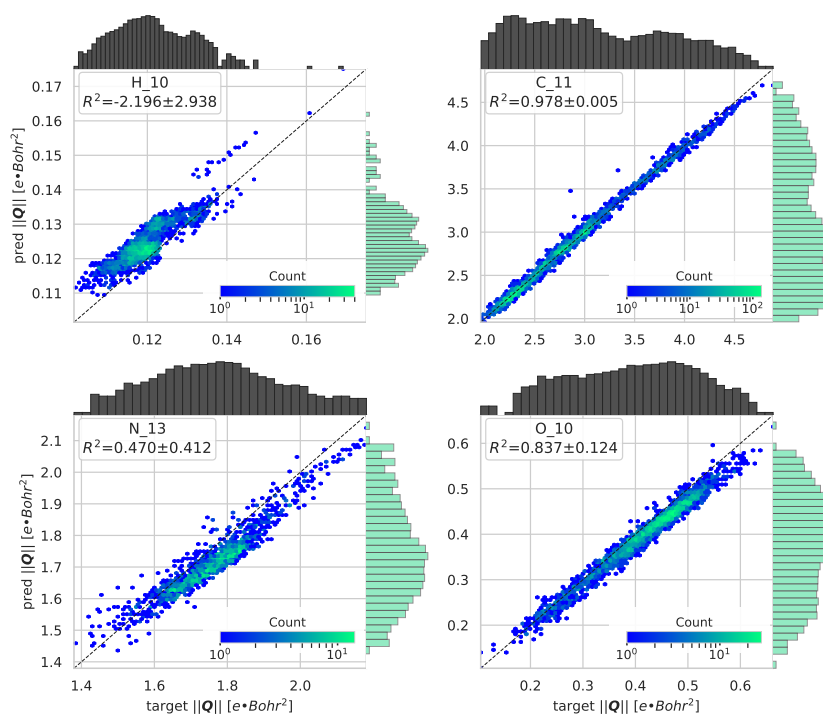


Figure 16: Parity plot for the OOD predictions of QT-Net for atomic quadrupole moments.